PHYSICAL REVIEW E VOLUME 55, NUMBER 4 APRIL 1997

Oscillations and spatiotemporal chaos of one-dimensional fluid fronts

D. P. Vallette, G. Jacobs, and J. P. Gollub
Physics Department, Haverford College, Haverford, Pennsylvania 19041
and Physics Department, University of Pennsylvania, Philadelphia, Pennsylvania 19104

(Received 11 September 1996)

The bifurcations to time-dependent and chaotic one-dimensional fluid fronts are investigated in the flow of a fluid inside a partially filled rotating horizontal cylinder. A primary cellular pattern undergoes a variety of secondary transitions, depending on the filling fraction. We document three types of transitions to time dependence which are shown to be qualitatively distinct by space-time Fourier analysis. We focus particularly on a highly symmetric transition to spatially subharmonic oscillations that is well represented by model equations. A subsequent transition of the oscillatory state to spatiotemporal chaos is explored quantitatively through the use of spectral analysis and complex demodulation to extract slowly varying amplitudes and phases. Many features of this chaotic state are at least qualitatively described by the model, including propagating compressions that are related to a locally depressed amplitude of oscillation. We are able to measure some of the parameters of the model directly. We also attempt to determine all of them by a least squares fitting method in the chaotic regime. Though this method is shown to work well for numerically generated data, experimental noise limits its use with experimental data. [S1063-651X(97)09104-6]

PACS number(s): 47.20.Lz, 47.52.+j, 47.54.+r

I. INTRODUCTION

Transitions to spatiotemporal chaos, which often occur beyond a secondary threshold, are challenging to describe and understand. Many examples of spatiotemporal chaos (STC) in one dimension have been studied both experimentally and numerically [1]. When the transition to STC occurs from a state that has a considerable degree of symmetry, a generic description may be possible by using model equations whose form is determined largely by symmetry considerations [2]. In a few cases, a close correspondence between model equations and experiments has been found, e.g., for convection in binary mixtures [3] and in electroconvection [4]. However, in many cases even a qualitative understanding of the spatiotemporal dynamics is missing.

Pattern-forming instabilities of cellular fronts are an attractive context for exploring the modeling of STC, because the full space-time behavior of the dynamical variables can be measured. The evolution of a one-dimensional fluid front inside a horizontal rotating cylinder is investigated in this study, which extends preliminary work published earlier [5]. Investigations in this system have shown it to be a rich pattern-forming system with a variety of transition sequences, depending on experimental parameters [6]. We focus especially on the transition to STC via spatially subharmonic oscillations (SSO) of cellular fronts, because it has well-defined space-time symmetries, and is amenable to modeling. We also describe an additional transition via an oscillatory state whose wavelength is apparently irrationally related to that of the base pattern; this phenomenon is observed near the SSO state in parameter space, but has different symmetry. We have fully characterized these transitions using a variety of methods, using space-time spectral and correlation analysis, and complex demodulation (see, e.g., [3].)

Because the flow has a free surface whose shape is complicated and time dependent, it is not realistically possible to utilize the full hydrodynamic equations to describe it. Two theoretical models have been proposed that are consistent with the basic symmetries of the problem. The first and more general of these models [7,8] considers the dynamics near a codimension-two point of a Turing (cellular) mode and a Hopf (oscillatory) mode. A number of interactions between these two modes are described, including a spatially subharmonic oscillation that grows supercritically as a secondary instability above the onset of the cellular state. This ‘‘sub-T’’ model is described by three complex amplitudes: that of the cellular state, and two amplitudes to characterize the opposite parity traveling waves, which together form the Hopf mode. A reduced model is applicable in cases where the secondary bifurcation is to a *stationary* Hopf mode and is observed at finite amplitude of the cellular state. In this case, the required variables are the phase ϕ of the base cellular state, and the complex amplitude of oscillation A. We will call this the ‘‘A-ϕ model.’’ This reduced form describes one of the generic symmetry-breaking bifurcations proposed by Coullet and Iooss [2] and has been investigated in detail in the context of one-dimensional Rayleigh-Bénard convection [9]. In a previous Brief Report, we have shown that some features of the transition to STC are captured by this model, and we present an extension and fuller discussion of this work here.

A main point of this investigation is to address the following question: How can one empirically test the adequacy of a model for the onset of STC? Several different methods are utilized, including methods of obtaining individual model coefficients. One novel approach is to attempt to fit the experimental chaotic data to the model (i.e., to determine the best fitting coefficients in a least squares sense), as has been recently demonstrated for temporal chaos by Baker, Gollub, and Blackburn [10]. Such an approach has not yet been tested for STC. We show here that this can be done for noise-free data obtained from simulations, but that the noise present in experimental data, at least in the present case, is a

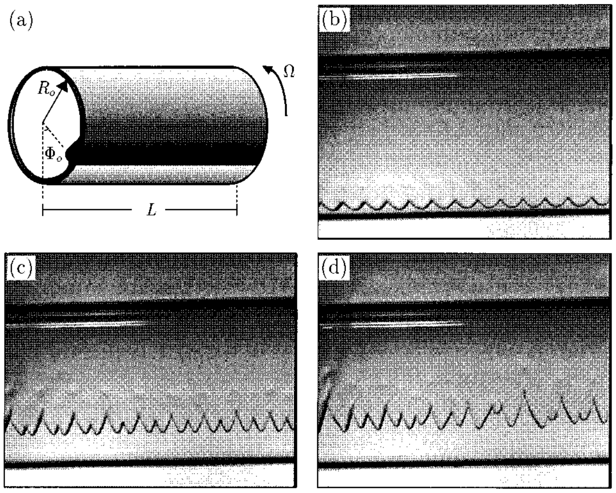

FIG. 1. (a) Diagram of the experimental geometry. The relevant dimensions are the cylinder radius R_0 and length L. The experimental parameters are the fluid volume fraction V, rotation rate Ω, and viscosity ν. See Sec. III for details. The angular position $\Phi_0(x,t)$ of the falling front exhibits highly symmetric stationary and time-dependent patterns. (b) Cellular, time-independent pattern; (c) spatially subharmonic oscillatory state; and (d) spatiotemporally chaotic state.

daunting obstacle. Therefore other more indirect methods have to be used. We are able to establish that many qualitative features of the transition to STC are represented adequately by the reduced two-field model.

The paper is organized as follows. In Sec. II the rotating rimming flow and earlier related experiments are described. The experimental and analysis methods are described in detail in Sec. III, including the process of complex demodulation. The phase diagram showing stability of time-independent and time-dependent patterns is presented in detail in Sec. IV, together with general stability measurements and statistical studies of the chaotic state. In Sec. V a detailed description of the reduced A-ϕ model is provided, together with experimental measurements of several of the model coefficients. The results of a least squares fitting method applied directly to the chaotic state are detailed in the Appendix. The discussion and conclusion follow in Sec. VI.

II. BACKGROUND

The system under investigation is fluid partially filling a horizontal rotating cylinder [Fig. 1(a)]. The relevant parameters are the filling fraction of fluid V, the fluid viscosity ν, the radius of the cylinder R_0, and the driving rate Ω (rate of rotation of the cylinder about its axis). We consider only the case of small V. Over a broad range of parameters, the observed behavior is characterized by dynamics on length scales much smaller than R_0, but larger than the mean film thickness. A characteristic length scale h for the flow can be found by identifying the film thickness at which gravitational and viscous forces would balance. This occurs when $\nu\Omega R/h^2=g$, so that $h=\sqrt{\nu\Omega R/g}$. The Reynolds number based on this scale is $\mathrm{Re}=(R_0\Omega h)/\nu$. In addition to h other length scales may be defined, including the mean film thickness based on fluid volume (a function of both R_0 and V). Because h may not be the only relevant scale, we leave the wave numbers characterizing flow structures as dimensional quantities.

We consider variations in V and Re primarily. In the limit of low driving rates most of the fluid forms a pool in the bottom of the cylinder, leaving a thin film of fluid that wets the inside of the cylinder everywhere. As the driving rate is increased, fluid is carried up the rising side of the cylinder where it subsequently falls, cascading back down to the pool.

At still higher Re, the pool is dragged up the rising side to a new equilibrium position, the state depicted in Fig. 1(a). The lower edge of this pool curves sharply into the fluid layer beneath it, and forms a linear front whose azimuthal position Φ_0 can be measured as a function of space and time. For a wide range of fluid volumes Φ_0 is homogeneous in the axial direction for a finite interval of driving rates. This homogeneous front (termed a flat front) may become unstable to traveling pulses or may give way to a cellular pattern. The traveling pulse state was investigated by Melo and Douady [11], who found that the density of traveling pulses increases as a function of Re, until eventually a stationary cellular pattern is formed. For larger V the flat front bifurcates instead directly to a uniform cellular pattern through a second order transition. This pattern is shown in Fig. 1(b). As Re is increased, the cellular pattern bifurcates to an oscillating state with twice the original wavelength (dubbed a spatially subharmonic oscillation). This regime is shown in Fig. 1(c); a preliminary study of this regime was reported in Ref. [5]. Further increase in Re leads to a regime of spatiotemporal chaos [Fig. 1(d)] that we explore in greater depth in this paper. There are actually several distinct types of spatiotemporal chaos, and we describe the differences between them in Sec. IV.

A number of investigators have explored some features of this system theoretically. The earliest report describing these instabilities was by Karweit and Corrsin [12], who reported a cellular instability. No attempt was made at that time to explain the phenomena, although a series of analytical and numerical studies of the high rotation rate limit were given by Ruschak and Scriven [13] and by Orr and Scriven [14]. Attempts to find solutions to the hydrodynamic equations as the driving rate is reduced have revealed singular points in parameter space where numerical results fail to converge. These singularities may be the result of multiple solutions as would be expected for a recirculating flow [15]. Johnson [16,17] carried out an analysis for both Newtonian and non-Newtonian fluids, starting from the lubrication approximation of the hydrodynamic equations. He was able to demonstrate the presence of a recirculating zone and several possible flow configurations, but could not provide predictions for the transitions to these solutions. Other viscoelastic studies of the coating flow both inside and outside of a rotating cylinder were conducted by Preziosi and Joseph [18], and by Sanders, Joseph, and Beavers [19]. Melo [20] investigated experimentally the applicability of the lubrication approximation to the flow in the low fluid volume limit.

An alternative to lubrication theory is a stream function approach to the two-dimensional steady-state problem. Chicharro and Peralta-Fabi [21] have solved the flow at low and high rotation rate limits for $V=0.5$ using stream functions, but note that numerical integration is necessary to solve for more specific flow configurations. In any case, current analysis does not provide a prediction for the primary instability to a cellular state which has been well documented experimentally over a broad range of fluid volumes and viscosities.

In addition to the states described in this article, there are a large number of dynamic and stationary states which have been documented. A systematic description of the parameter space was conducted recently by Thoroddsen and Mahadevan [6] for a wide range of fluid volumes and viscosities. Many of these phenomena appear to be the result of free surface instabilities, and warrant more detailed investigation.

III. EXPERIMENTAL AND ANALYSIS METHODS

The apparatus used for this experiment is illustrated in Fig. 1(a). A glass cylinder of radius $R_0=5$ cm and length $L=50$ cm is partially filled with silicone oil of viscosity $\nu=10$ cS. Typical filling fractions are in the range 0.01–0.04. The typical mean thickness of the wetting film is about 0.06 cm. In order to obtain spatially uniform patterns, the cylinder must have a uniform radius. The radius of the cylinder was fixed by the manufacturer by shrinking the glass (thickness 1/4 in.) onto a custom ground mandrill, and the exterior was ground and polished concentrically, to within 0.005 cm. End caps were machined from Delrin, and contain a double O-ring seal. One end cap is coupled directly to a microstepping motor (4000 microsteps per revolution). The other end cap provides access to the fluid through an opening. Some of the critical values of Re for transitions vary substantially with temperature. In order to ensure repeatability, the cylinder is contained within a well-insulated box maintained at fixed temperature ($T=25.0\pm0.2$ °C).

Control of the rotation rate is provided by a GPIB connection to a signal generator driving the stepping motor. In this way, incremental sweeps of Re with arbitrary step size (in Re) can be performed to automate the data collection process. Transitions are determined with step sizes of 0.002 near the transitions, followed by wait times of 300 s to allow a steady state to be achieved.

The fluid front has sharp curvature [Fig. 1(a)] so that a uniform lighted background produces a strong contrast; this makes the determination of the front position possible. Front finding is performed in real time using a Data Raptor image capture board [22]. Pixel values can be read from the board as the image is being written to the board. A Cohu charge-coupled device (CCD) camera is used to obtain digitized images with resolution of 640×480 pixels. The full length of the horizontally oriented cylinder is captured. Typically, this corresponds to 30–40 cellular wavelengths. The height of the cellular front pattern $U(x,t)$ is typically 30 pixels vertically. Since angular displacements Φ_0 of the front actually follow a circular path, one must take care that the circumference of the cylinder is tangential to the plane that is imaged, at the location of the mean front.

One may take advantage of available processing time to improve the vertical resolution of the position of the front. A vertical line of intensity values is read for each horizontal point in the frame buffer. The first spatial derivative of these data shows a large negative peak at the point of greatest contrast. The centroid of this peak is defined as the position of the front, and is insensitive to the range of integration. In this way, the position of the front at each time t, $U(x,t)$ can be obtained reliably to within 0.2 pixels of vertical resolution. Data are captured at 30 Hz and are written to disk continuously to allow the capturing of data records of arbitrary length.

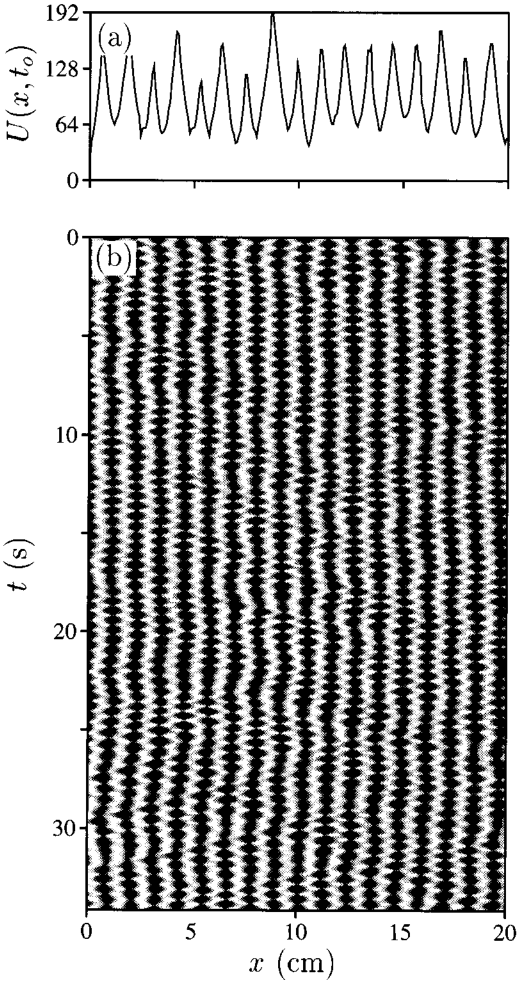

FIG. 2. (a) Enlargement of the front position $U(x,t_0)$ (a projection of Φ_0 onto the imaging plane) for the weakly chaotic state, in arbitrary units. The spatially subharmonic structure is evident in the left half of the image. (b) Gray scale space-time plot of the weakly chaotic state; dark regions correspond to large U. Both the amplitude of the oscillation and the wavelength of the cellular structure fluctuate slowly in space and time ($V=0.032$, Re=95.13).

A typical example of the digitized front height $U(x,t)$ at an arbitrary time is shown in Fig. 2(a). For clarity, only a portion of the cell is shown. This state is typical of the weakly chaotic spatially subharmonic state (SSO) shown in Figs. 1(c) and 1(d). The spatially subharmonic structure is clearly evident from the alternate high and low amplitude peaks in the left part of the figure. The right side of the cell does not show the subharmonic structure in this instant, because the oscillations at this time are out of phase with those of the left side of the cell. The time dependence of the pattern is shown in Fig. 2(b), where the spatially subharmonic oscillations are evident from the checkerboard pattern of the

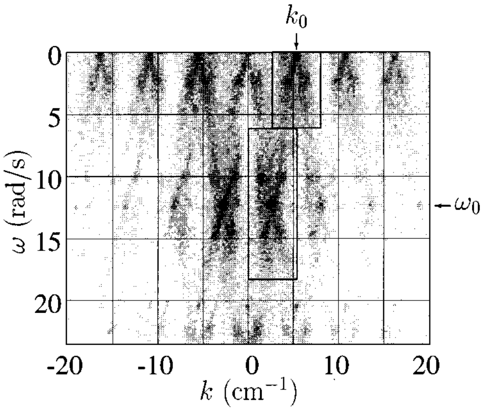

FIG. 3. Power spectrum $P(k,\omega)$ of the data in Fig. 2. The sharply defined peaks are well separated in Fourier space. Boxes surrounding the primary peak ($k=k_0=\pm 5.5$ cm^{-1}, $\omega=0$ rad/s) and the subharmonic peak ($k=2.7$, cm^{-1}, $\omega=\omega_0=11.9$ rad/s) define the demodulation window for the slowly varying amplitudes U_0, and A, respectively.

dark peaks. (Alternate peaks in the pattern are oscillating with opposite phase.) Dark regions correspond to large U.

Spatial variations in the phase and amplitude of the oscillations and in the wavelength of the cells generally occur on a length scale larger than that of the wavelength of the pattern, and may therefore be defined as slow perturbations of the basic state. The separation of scales is evident in the power spectrum $P(k,\omega)$ (the magnitude squared of the space-time Fourier transform), which is shown in Fig. 3. This spectrum was performed over 512 points in space (40 cm) and 2048 points in time (68 s). The size of the data record limits the resolution to approximately 0.16 cm^{-1} in wave number and 0.092 rad/s in angular frequency. The most prominent peaks occur at ($k=\pm 5.5$ cm^{-1}, $\omega=0$ rad/s) and at ($k=2.7$ cm^{-1}, $\omega=11.9$ rad/s). These peaks are sharp and well separated in ω-k space. These features allow U to be expressed as a sum of low order modes in k and ω with slowly varying amplitudes. The first mode U_0 (taken to be real) corresponds to the stationary cellular part of the pattern of wave number k_0 and the subharmonic mode A corresponds to the amplitude of the oscillations of wave number $k_0/2$, and frequency ω_0. That is,

$$U(x,t)=U_0 e^{i(k_0 x+\phi)}+A e^{i\omega_0 t} e^{i(k_0 x/2+\phi)}+\text{c.c.}+\cdots, \quad (1)$$

where U_0 and ϕ are slow real functions of x, t, and A is slowly varying but complex. The slowly varying amplitudes U_0, A, and ϕ are obtained by complex demodulation, in order to compare the dynamics with the predictions of model equations (see Sec. V). This process consists of applying a rectangular window in k-ω space, followed by a back transform to x-t space. Demodulation windows are chosen so as to retain the largest possible bandwidth, as shown by the boxes around the primary and secondary peaks in Fig. 3. The boxes shown are of size $2(dk)=2.7$ cm^{-1}, by $2(d\omega)=11.9$ rad/s.

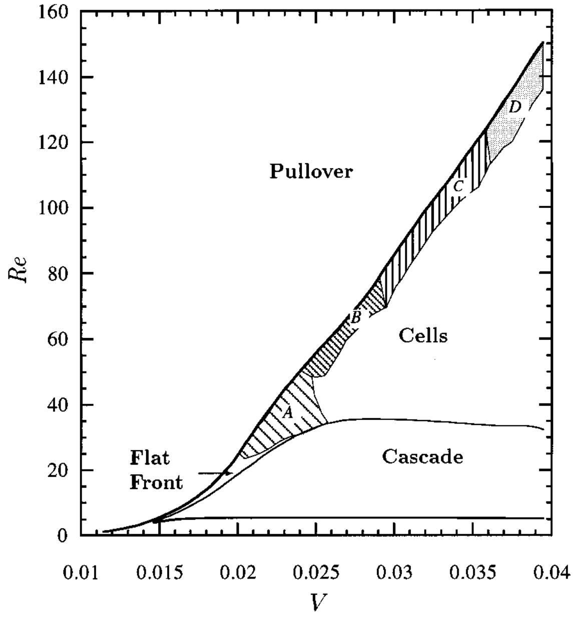

FIG. 4. Phase diagram of stable states of the front. At low Re, a pool of fluid forms in bottom of the cylinder. As Re increases, perturbations of the pool form as fingers of thickened fluid, and lead to a cascade of fronts. At still higher Re, transitions occur to a flat or undulating front (below region A), or to a cellular state. Four additional dynamical regimes are observed in this phase space: Region A, a traveling pulse state; region B, a chaotic state marked by wave-number fluctuations in the cellular pattern and unstable subharmonic oscillations; region C, the spatially subharmonic state (SSO), together with transitions to spatiotemporal chaos; and region D, a state in which oscillations are incommensurate with the cellular pattern.

IV. PHASE DIAGRAM, WAVE-NUMBER DEPENDENCE, AND STATISTICAL STUDIES

A. Phase diagram in Re-V space

A phase diagram of the various pattern-forming states is shown in Fig. 4 for 10 cS silicone oil as a function of Reynolds number and volume fraction. Stability boundaries were measured by slowly increasing Re at fixed V. For Re near zero, a pool of fluid forms a uniform front with no discernible surface perturbations. A transition to cascading from this state is independent of fluid volume over most of the parameter space explored. It is a weakly hysteretic transition, with a hysteresis of no more than 2% of the critical Re. The cascading state disappears at much higher viscosities, and the transition then occurs directly from the uniform front to the cellular state [21]. Thus the system (and especially the cellular instability) may be easier to model in the high viscosity limit.

Beyond the cascading region (i.e., at higher Re) either a flat front or a cellular state emerges, depending on the filling fraction V. For V in the range $0.15 \lesssim V \lesssim 0.23$ the cascading state is replaced by a flat front. For small V in this range, the flat front may appear to undulate slowly. Traveling pulses, reported previously [11], occur in region A.

For $V \gtrsim 0.025$ the cascading region is replaced by a small amplitude cellular state. There is an overlap in stability be-

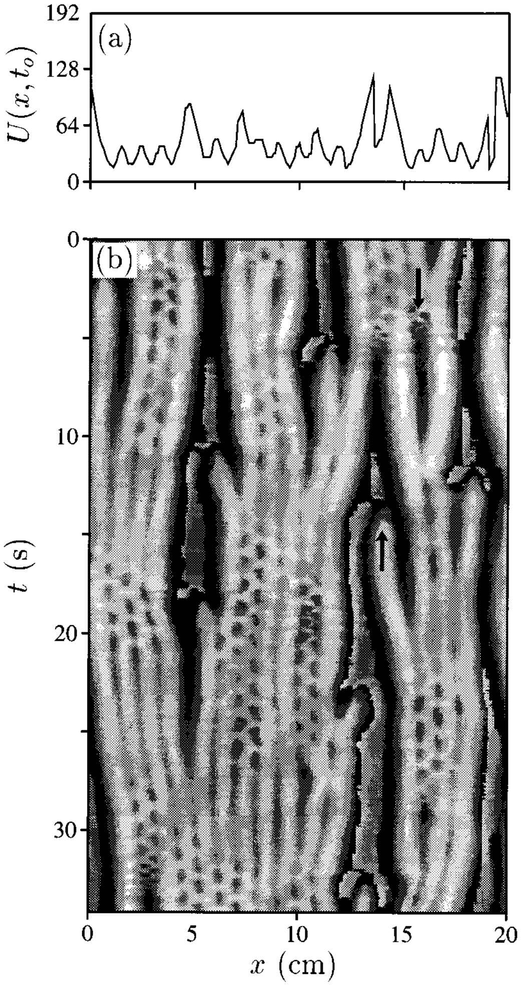

FIG. 5. The chaotic state observed in region B of Fig. 4. (a) Front position $U(x)$ at an arbitrary time and (b) gray scale space-time diagram. A localized spatially period doubled oscillation of the pattern is observed when the pattern is briefly compressed. Cell nucleation and annihilation events are indicated by the arrows ($V=0.028$, Re=60.03).

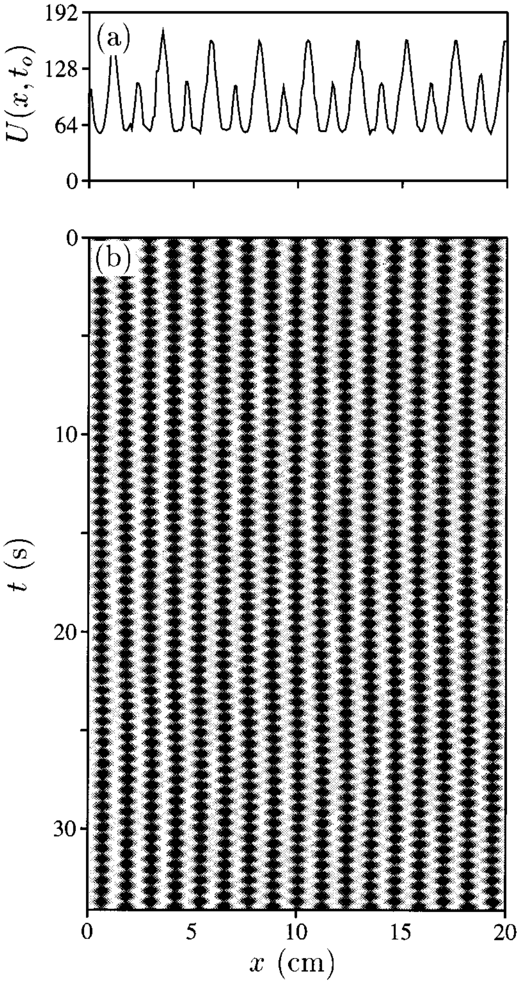

FIG. 6. The space and time periodic SSO state (region C of Fig. 4.) (a) Front position $U(x)$ at an arbitrary time and (b) gray scale space-time diagram ($V=0.032$, Re=92.43).

tween the flat front and the cascading state near the boundary of the cellular state, and the flat front region is not shown in the stability diagram. To find the flat front it is usually necessary to begin from the cellular state and lower the driving rate. The cellular state is stable over a broad range of Re. Its stability has been reported in a number of investigations [5,6,17,21], although a satisfactory explanation for this primary instability is still lacking.

At the upper stability limit of the cellular state, various transitions to increasing disorder in space and time are observed. Three distinct dynamical regimes are examined in this study, labeled B, C, and D. In region B, fluctuations in the wave number of the pattern are observed, together with cell nucleation and annihilation events. An example of a space-time diagram for this region is shown in Fig. 5. Figure 5(a) shows a typical snapshot of this state at a fixed time. Structures of different length scales and amplitudes coexist, and evolve in time as seen in Fig. 5(b). Cells may be compressed or stretched, a process that leads to cell nucleation or annihilation events. When the wavelength is sufficiently small, a localized spatially subharmonic oscillation of the peaks is observed, similar to those in Fig. 1(c). The strong wavelength dependence of the oscillation amplitude is also observed in region C of Fig. 4, as we discuss in Sec. IV B.

In region C, the SSO state is stable and the oscillations fill the length of the cell (see Fig. 6). As the driving rate is increased, the behavior of the oscillatory state becomes chaotic in space and time, with distinct ''weak'' and ''strong'' chaotic states (depending on whether cell nucleation events occur) as reported by Vallette, Edwards, and Gollub [5]. These states are analyzed more fully in the present paper. A space-time diagram for the strongly chaotic state is shown in Fig. 7. When the wavelength is sufficiently large, the oscillations cease.

At still higher fluid volumes an oscillatory instability of the cellular state is observed whose wavelength is *not* a subharmonic of the basic pattern (region D of Fig. 4). An example of this state is shown in Fig. 8. The dynamics of the two amplitudes A and U_0 may not be as strongly coupled here as they are in the case of the SSO state (Fig. 2).

The distinction between the three dynamical regions is

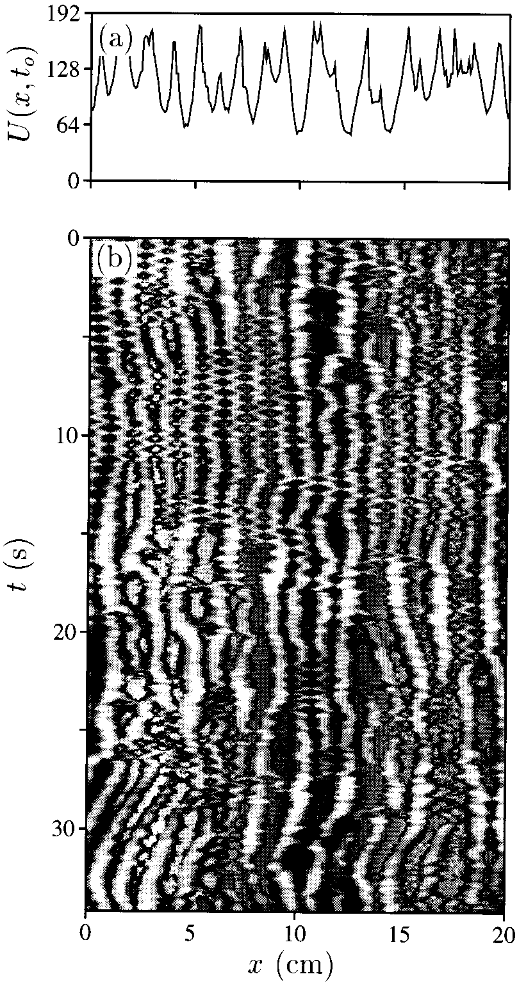

FIG. 7. The strongly chaotic SSO state (upper part of region C, Fig. 4). (a) Front position $U(x)$ at an arbitrary time and (b) gray scale space-time diagram. Nucleation and annihilation events are evident as for region B ($V=0.032$, $\mathrm{Re}=98.26$).

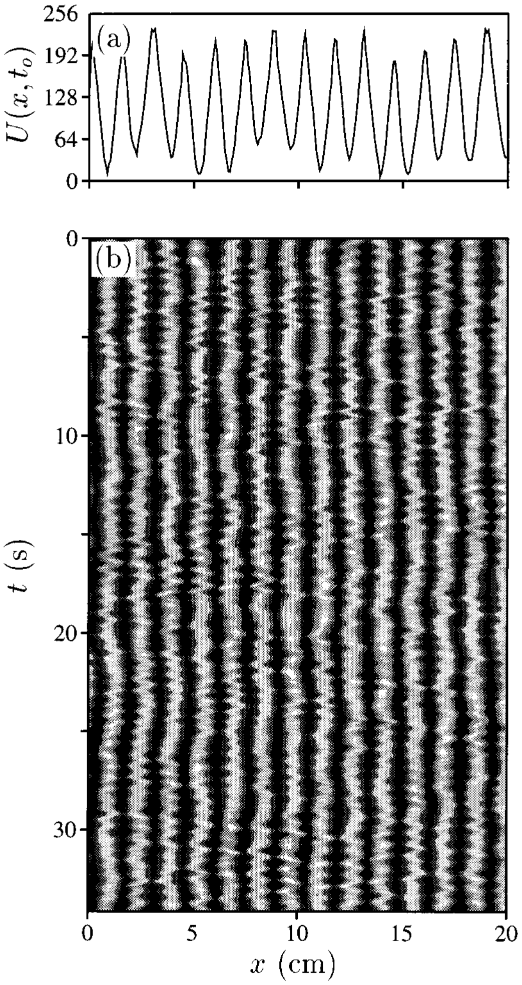

FIG. 8. The disordered oscillatory state (region D of Fig. 4). (a) Front position $U(x)$ at an arbitrary time and (b) gray scale space-time diagram. The wavelength of the oscillatory mode is not well defined, and is clearly not a subharmonic of the cellular state ($V=0.040$, $\mathrm{Re}=149.00$).

even more apparent when one considers their power spectra in the two-dimensional frequency-wave-number domain as shown in Fig. 9 (and Fig. 3). Figure 9(a) corresponds to the first of the chaotic states (region B), and shows a power spectrum for which no primary peak at $\omega=0$ is distinguishable. This is reflected in the dynamics of Fig. 5, where the wavelengths of individual cells vary continuously. At higher V (Fig. 3) the cellular state is more stable, and the primary peak corresponding to it at $\omega=0$ is clearly evident, as is the subharmonic peak A, which is sharply defined and has a wavelength clearly commensurate with that of U_0. However, the oscillations in region D [Fig. 9(b)] fill out lines (rather than isolated points) at finite ω in the ω-k plane; these oscillations are generally not commensurate with U_0. Quasiperiodic incommensurate states have been discussed by Coullet and Iooss [2].

In each of the cases examined, there is an upper limit (in Re) to the stability of any front at all (even time dependent); this limit is represented by the dark solid line in Fig. 4. Above this line the fluid in the front region is pulled over the top of the cylinder and the front is no longer identifiable.

B. The wave-number dependence of the cellular and oscillatory states

In order to address the transition to spatiotemporal chaos of Fig. 2, it is first necessary to consider the stability of the steady cellular (SC) state. The wave-number range of the SC state is shown via the stability diagram in Fig. 10. The mean wave number $\langle k \rangle$ is calculated over the middle 50% of the image. The wave number of a given pattern is not easily controlled in this system; thus a systematic search of Re-k space is difficult. A wave number different from the most rapidly growing mode k_c at the onset of U_0 can be obtained by taking finite size steps across a stability boundary from below or above, to enter the regime of the steady cellular pattern. Steps from the flat front tend to give patterns with a high wave number, whereas steps from the time-dependent regime, and especially from the strongly chaotic state, may result in wave numbers smaller than k_0. In the strongly chaotic state fluctuations in the number of cells are large, and hence a wide range of $\langle k \rangle$ can be achieved by quenching.

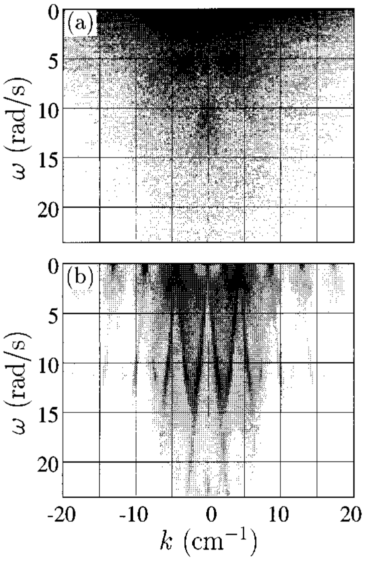

FIG. 9. Power spectra of the data representing states in regions B,D of Fig. 4. (a) The unstable oscillations seen in Fig. 5 form a broad peak at finite frequency. The fluctuations in wavelength and in the number of cells cause the peak at $\omega=0$ to be extremely broad. (b) The oscillatory state corresponding to Fig. 8 and region D of Fig. 4 does not have a well-resolved peak at finite frequency, and its wavelength is apparently not a harmonic of that of the cellular pattern at $k=4.5\ \mathrm{cm}^{-1}$.

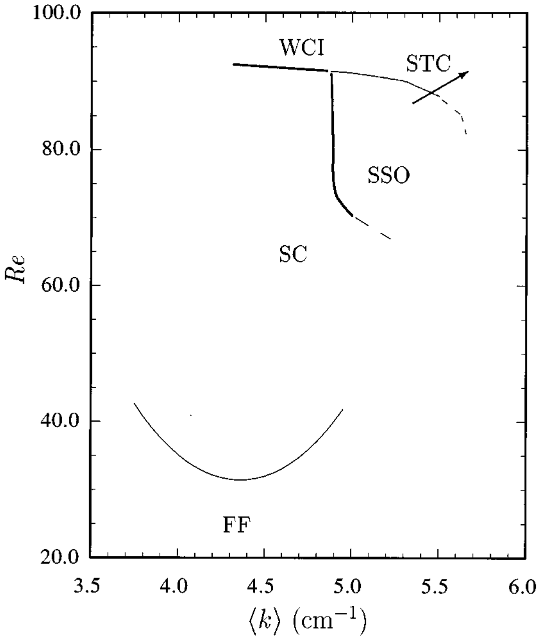

FIG. 10. Stability diagram for the cellular and subharmonic oscillatory (SSO) states (region C of Fig. 4) as a function of mean wave number $\langle k\rangle$. The stationary cellular state (SC) emerges supercritically from a flat front (FF) at $\mathrm{Re}_c=31.18$, $k_c=4.4\ \mathrm{cm}^{-1}$ ($V=0.032$). Near this point, a broad range of wave numbers are stable. An Eckhaus instability is approximated by the parabola shown. A wavelength-changing instability (WCI) is observed at the upper limit of the cellular state. A ramp of Re across this boundary drives a cellular pattern to a state with strongly compressed wave number $\langle k\rangle$ in the spatiotemporally chaotic region. A second instability of the SC state is to spatially subharmonic oscillations for higher wave numbers. The SSO state also exhibits wavelength-changing behavior and may cross the line to a chaotic state continuously as indicated by the arrow ($V=0.032$).

Once a particular wave number is selected in the SC state, the system will remain at that wavelength, provided it lies well within the stability boundaries for that state. Through these and similar techniques, a profile for the stable wave-number range of the SC state may be constructed, as is shown in Fig. 10.

An estimate for the parabolic curve corresponding to the Eckhaus boundary of the cellular state is plotted at the bottom of Fig. 10. Because strong control over the wave number is unavailable, a precise determination of the Eckhaus boundary is not possible. The curve shown corresponds to a parabola accommodating the lowest values of Re observed in many runs. The cellular front undergoes a long wavelength instability characteristic of the Eckhaus transition if Re is reduced below this curve.

A second wavelength-changing instability (WCI) is observed at large Re and bounds the SC state from above. This transition leads to a discontinuous increase in the wave number of the system. This sudden shift in k takes SC states of the system into the weakly chaotic (STC) range [23]. An example of this transition is shown in Fig. 11. At $t=0$ s the system is in the SC state with an initial wave number $k=4.32\ \mathrm{cm}^{-1}$. At $t=17$ s, Re is stepped from 92.42 by an upward step of $\Delta\mathrm{Re}=0.20$. After a brief time (whose duration depends on $\Delta\mathrm{Re}$) the widths of the cells begin to fluctuate; these fluctuations travel through the system and grow until they become large enough to cause cell nucleation events. Along with these fluctuations one begins to see the emergence of oscillations. Eventually the system stabilizes at a new higher wave number and (chaotic) oscillations permeate the system.

End effects also affect the wavelength of the pattern and the stability of the SC state. If the wavelength of the pattern is sufficiently large (or sufficiently small), cells may be nucleated (or removed) at the bounding end caps of the cylinder. These result in a local gradient in the phase of U_0 which slowly diffuses through the system. The time scale for this process is roughly 1–30 min, depending on how far the state is from k_c. As the driving rate is increased, the SC state becomes increasingly stable against wavelength perturbations and these events are less frequent.

The WCI transition led us initially to suspect that the transition to time dependence was invariably subcritical, with a coexistence of the SC and chaotic states. However, a broader search of the Re-k plane shows that the transition to oscillations is continuous at higher $\langle k\rangle$. The transition between the SC state and the SSO state is represented in Fig. 10 by the steep downward sloping curve separating the SSO and SC states. Due to the steepness of the curve, it is difficult to find wave number k for which the transition will be continuous as Re is increased. Instead, one may cross the stability boundary horizontally by taking advantage of the slow decrease in k of the cellular pattern for a range in Re where the SSO state is homogeneous and the oscillations are steady.

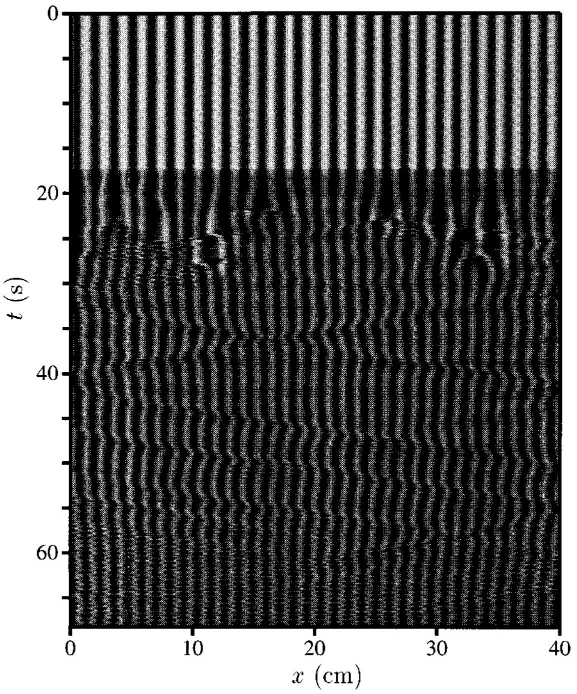

FIG. 11. Gray scale space-time plot of $U(x,t)$ showing the WCI transition in Fig. 10. The system undergoes a transition from an initial $\langle k\rangle = 4.32\ \mathrm{cm}^{-1}$ to $\langle k\rangle = 5.56\ \mathrm{cm}^{-1}$, following an imposed step increase of Δ Re=0.20 from Re=92.42 at $t = 14$ s. Fluctuations in the wavelength of the cellular pattern grow and travel through the system, compressing the pattern, and causing the onset of weakly chaotic oscillations.

Evidence that this transition to subharmonic oscillations is continuous is shown in Fig. 12(a). In Fig. 12(a) the square of the amplitude is plotted as a function of wave number, averaged over the center 50% of the cell. The amplitude decays continuously to zero during this transition. The suppression of A for the points near $k = 4.80\ \mathrm{cm}^{-1}$ is the result of inhomogeneity in the oscillatory pattern. This sensitivity to small inhomogeneities in the system near the transition is characteristic of second order transitions. The Hopf frequency is shown in Fig. 12(b); it also varies smoothly near the transition. A further increase in Re may cause the SSO state to undergo a continuous transition to STC in which the wave number increases reversibly. This transition is indicated by the arrow in Fig. 10.

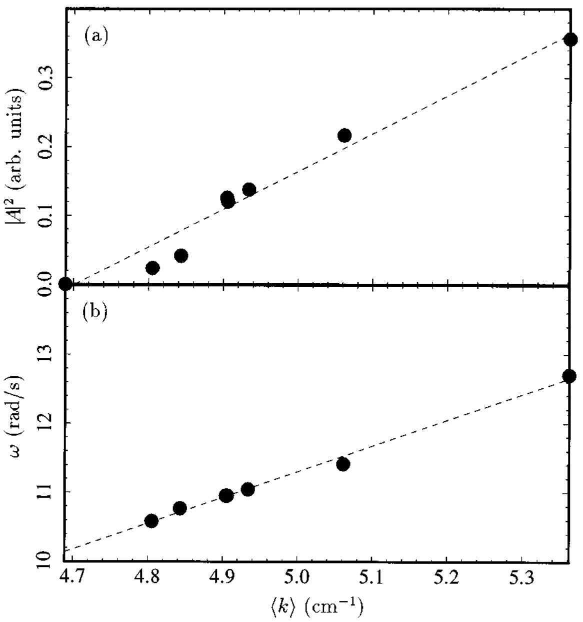

FIG. 12. Plots of the square of the oscillation amplitude $|A|^2$ and frequency ω as a function of decreasing $\langle k\rangle$ near the SC to SSO transition of Fig. 10. The transition exhibits the behavior characteristic of a second order transition. The slope of the ω-k curve gives an estimate for parameters in a model equation motivated by symmetry (Re=74.57).

C. Space and time scales for spatiotemporal chaos

A reversible transition from the SSO state to the chaotic regime via long wavelength perturbations, which occurs along the line indicated by the arrow in Fig. 10, leads to spatiotemporal chaos. In the preliminary report [5], the transitions observed in region C of Fig. 4 were quantified by measuring the decay of the correlation function of the front height U. In that investigation it was determined that the correlation time τ decayed more quickly with increasing Re than did the correlation length ξ. However, when one considers the sharp separation between peaks in the spectrum of U, it is apparent that two lengths and two time scales can be defined for the system, corresponding to the principal spectral peaks of U_0 and A. It is more direct to obtain length and time scales ξ and τ from the shapes of these peaks than it is to fit their correlation lengths. In this paper, we therefore define ξ and τ somewhat differently, as follows:

$$\xi^{-1} \equiv \delta k = \left(\frac{\sum_{\omega_0 \pm \Delta\omega} k^2 |U(k,\omega)|^2}{\sum_{\omega_0 \pm \Delta\omega} |U(k,\omega)|^2} \right)^{1/2}, \tag{2a}$$

$$\tau^{-1} \equiv \delta\omega = \left(\frac{\sum_{k_0 \pm \Delta k} \omega^2 |U(k,\omega)|^2}{\sum_{k_0 \pm \Delta k} |U(k,\omega)|^2} \right)^{1/2}, \tag{2b}$$

where the ranges of the sums $\Delta\omega$, Δk are the demodulation windows shown in Fig. 3.

As an example, consider the power spectrum $P(k)$ of the primary peak U_0 in Fig. 13(a), for two values of Re. This spectral distribution was obtained by integrating $U(k,\omega)$ over a window of size $\Delta\omega = 6.0$ rad/s centered at $\omega = 0$. Data were collected by sequentially increasing Re from a point near the oscillatory bifurcation to the loss of the front over the top of the cylinder. The solid squares correspond to Re =95.91 and the open squares to Re=98.26. The wave number is nondimensionalized by the wave number of the pattern in the time-independent state. In addition to a broadening of the peak of the cellular pattern, there is a slight increase in the wave number of the pattern with increasing Re. In order to find the width of the primary peak, both windowing and a

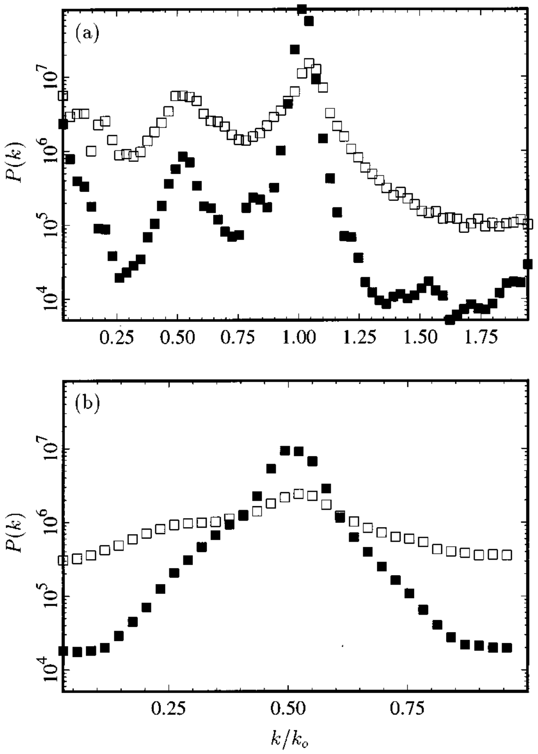

FIG. 13. (a) Spatial power spectra $P(k)$ of the weakly chaotic state of Fig. 2, and strongly chaotic state of Fig. 7 integrated over ω about $\omega = 0$. The primary peak near $(k_0,0)$ in Fig. 3 of the weakly chaotic state (Re=95.91—solid squares) is narrower than that of the strongly chaotic state (Re=98.26—open squares). The width of the peak defines the inverse of a correlation length that decreases with increasing Re. The growth of the subsidiary peak at $k/k_0 = 0.5$ is the result of annihilations resulting in a local wavelength doubling. (b) Power spectrum $P(k)$ for the finite subharmonic oscillatory peak near $(k_0/2,\omega_0)$ in Fig. 3.

thresholding routine were used to exclude data below a noise threshold. This method is effective when the peak is at least two orders of magnitude greater than subsidiary peaks and background noise, as for the data at Re=95.91. However, as Re is increased, cell annihilation events become common. In that case, the peaks are not adequately resolved, so that a precisely defined width is hard to measure at the largest values of Re. In the high Re range, the length and time scales of the subharmonic peak A may be more reliable. An example of $P(k)$ for the subharmonic peak is shown in Fig. 13(b). Here the subharmonic peak is resolved even for large values of Re.

The dependencies on driving rate of ξ^{-1} and τ^{-1} for the two spectral peaks are shown in Fig. 14. For this run, the initial wave number and Hopf frequency near the transition are $k_0 = 5.34\ \mathrm{cm}^{-1}$, $\omega_0 = 11.8$ rad/s. Circles correspond to the widths of the primary peak U_0 and squares to the widths of the spatially subharmonic peak A. This figure demonstrates that the transitions to disorder of U_0, A are strongly correlated, and that the loss of spatial order begins at a somewhat larger value of Re than does the loss of temporal order. An explanation of this transition which depends on the coupling between U_0, A is warranted, and is the subject of the next section.

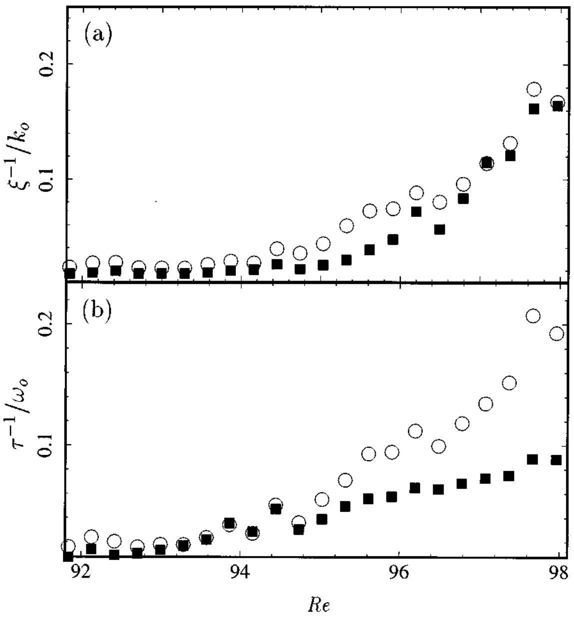

FIG. 14. (a) Characteristic inverse length scales ξ^{-1}/k^0 defined by the widths of the spectral peaks of Fig. 13 as a function of Re. The primary peak near $(k_0,0)$ and the subharmonic peak near $(k_0/2,\omega_0)$, represented by circles and squares, respectively, broaden in a similar manner. (b) Inverse time scales τ^{-1}/ω_0 for the primary and subharmonic peaks. The temporal correlations begin to decay at a lower value of Re than do the spatial correlations.

D. Demodulated fields

The strong correlation between base pattern and oscillation can be seen in the examples shown in Fig. 15. Figure 15(a) is a gray scale plot of the phase gradient $\partial\phi/\partial x$ of the front plotted in Fig. 2. Dark regions correspond to regions of increased wave number (local compression of the pattern) and light regions to reduced wave number (pattern stretching). These localized perturbations travel at constant speed (2.5±0.3 cm/s). Fluctuations in both the magnitude and the phase of the oscillation amplitude $A = \rho e^{i\psi}$ are correlated with these regions of stretching and compression of the cells. We present the magnitude $\rho(x,t)$ and the frequency variations $\partial\psi/\partial t$ in Figs. 15(b) and 15(c). The oscillation amplitude at this value of Re is fairly smooth, as fluctuations are relatively small, about 25% of the mean amplitude. The correlation between base pattern phase gradient and the oscillation amplitude is also observed in model equations by Lega and co-workers [9,24], and also occurs in the Nozaki-Bekki holes found in solutions to the complex Ginzburg-Landau equation [25].

By contrast, variations in the phase of A are large in this example. These large variations are seen in Fig. 15(c) as a transient slowing down and subsequent acceleration of the oscillations. These changes are correlated with a reduction and then an increase in the wave number. Recall that this sensitivity of the oscillation frequency to wave number was observed in the laminar state as well (Fig. 12.)

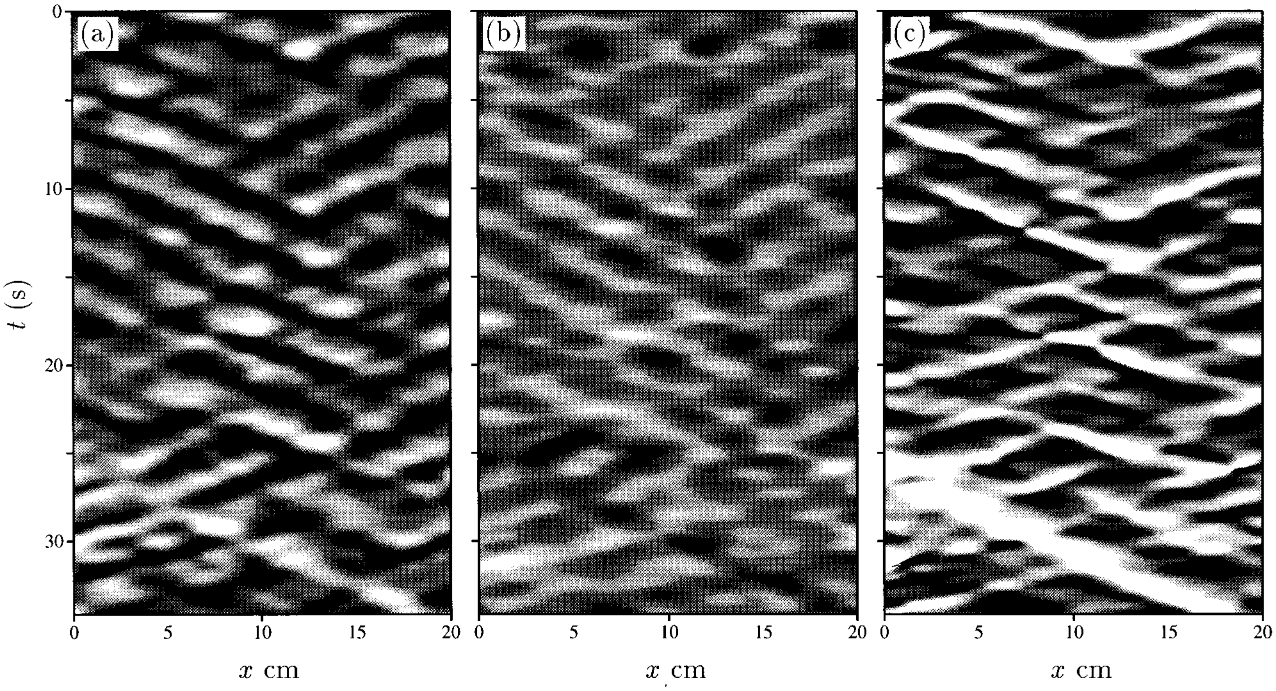

FIG. 15. Space-time plots of the demodulated fields corresponding to Fig. 2: (a) phase gradient $\partial\phi/\partial x$, (b) oscillation amplitude $|A|$, and (c) fluctuations in oscillation frequency $\partial\psi/\partial t$. The demodulation window used to define these amplitudes is shown in Fig. 3. The close coupling between the phases and the oscillation amplitude, and the traveling pulses in the phases, are qualitatively similar to features found in model equations.

V. COMPARISON TO A TWO-FIELD MODEL

A. Description of the model

The following features of the SSO transition may be adequately described by the two-field ''A-ϕ'' model proposed by Lega [24], and by Daviaud *et al.* [9]. The critical driving rate Re_0 and the frequency of oscillation ω both vary significantly with wave number. A spatiotemporally chaotic state grows from the oscillatory state in which fluctuations in ϕ and A are strongly correlated. These strong fluctuations travel at constant speed through the cylinder. Finally, the strength of the fluctuations increases with the control parameter, until eventually one observes nucleation and annihilation events, similar to intermittent bursting events observed in the model.

This two-field model supposes that the dynamics of the bifurcating state may be captured by an equation which couples the complex field A to the phase ϕ of the stationary cellular amplitude U_0:

$$\frac{\partial A}{\partial t}=\mu A+(1+i\alpha)\,\frac{\partial^2 A}{\partial x^2}-(1+i\beta)|A|^2A-(\gamma+i\delta)\,\frac{\partial\phi}{\partial x}\,A, \tag{3a}$$

$$\frac{\partial\phi}{\partial t}=\chi\,\frac{\partial}{\partial x}\,|A|^2+i\eta\left(\frac{\partial A}{\partial x}\,\bar{A}-\overline{\frac{\partial A}{\partial x}}\,A\right)+\kappa\,\frac{\partial^2\phi}{\partial x^2}. \tag{3b}$$

Time, space, and amplitude scales are chosen so as to set three of the coefficients to unity. Except for the last term, Eq. (3a) is of the form of a complex Ginzburg-Landau (CGL) equation, which is known to produce spatiotemporally chaotic data via an instability in the phase ψ of A (the Benjamin-Feir instability [26].) As in the usual CGL equation, a laminar nontrivial solution exists for $\mu>0$,

$$A(x,t)=A_0=\sqrt{\mu}e^{(-i\beta\mu t+i\psi_0)},\quad \phi(x,t)=\phi_0. \tag{4}$$

B. Experimental determination of parameters

Several properties of the laminar solution can be used to obtain numerical values of certain coefficients. The coefficient of the coupling term $\gamma+i\delta$ can be determined by measuring the wavelength dependence of ω and the critical driving rate for the transition Re(k). Note that Eq. (3b) is invariant under an overall compression of the pattern $\phi_0\rightarrow\phi_0+qx$, where $q=k-k_0$. Under this transformation, the oscillation frequency is offset by an amount proportional to q, $\omega\rightarrow\omega+(\beta\gamma-\delta)q$. The effect of varying q on amplitude and frequency of the laminar state was shown already in Fig. 12 of Sec. IV B. The slope of the best fitting line in Fig. 12(b) gives $\beta\gamma-\delta=3.73\pm0.13$ cm/s. Estimates for β and γ allow a determination of δ independently (see below). Physical units are used for all measured coefficients because the diffusion coefficient α_r for A is not known.

The bifurcation parameter μ is also offset by an amount proportional to q when the pattern is compressed: $\mu\rightarrow\mu-\gamma q$, and therefore $|A_0|^2=\mu-\gamma q$. One may assume Re to be linearly proportional to μ for fixed k. Under this assumption, the line of marginal stability for the oscillations is defined by

TABLE I. Coefficients of the model obtained by independent measurements on the laminar oscillatory state.

Coefficient	Measured value
β_i	$-7.2\,\pm\,1.6$ rad/s
γ	$1.03\,\pm\,0.21$ cm
δ	$-11.1\,\pm\,1.6$ cm/s[a]
$a_1=\beta_i\gamma-\delta$	$3.73\,\pm\,0.13$ cm/s

[a] δ was calculated from measured values for β_i,γ,a_1.

$$\mu(q)=\frac{\mathrm{Re}(q)-\mathrm{Re}_0}{\mathrm{Re}_0}=0,$$

where Re_0 is defined for an arbitrary choice of k_0. Then,

$$\gamma=-\frac{\partial\mu^*}{\partial q}=-\frac{1}{\mathrm{Re}_0}\frac{\partial\,\mathrm{Re}}{\partial k}.$$

That is, it is proportional to the slope of the marginal stability curve for oscillations in the k-Re plane. A natural choice of k_0, Re_0 is the point of intersection of the WCI boundary and the SSO boundary at (4.82 cm^{-1}, 88.30). With this choice, we find that $\gamma=1.04\pm0.08$ cm. Here the boundary is defined by the points in the SC state with the highest wave number at a given Re beyond which oscillations are observed.

The oscillation frequency is also predicted to vary with μ by Eq. (4). That is, ω is expected to vary as $\omega=\omega_0-\beta\mu$, for fixed k, or

$$\beta=-\left(\frac{\partial\omega}{\partial\mu}\right)_k=-\mathrm{Re}_0\left(\frac{\partial\omega}{\partial\,\mathrm{Re}}\right).$$

To obtain β, the frequency of oscillation of the SSO state was measured as a function of increasing μ. From this measurement, we find $\beta=-7.2\pm0.8$ rad/s. Given these values of γ and β we obtain $\delta=-11.1\pm1.4$ cm/s. Estimates of the other model coefficients require an imposition of spatial variations on the pattern, and such experiments have not been performed directly. The coefficients so far determined are summarized in Table I. In the Appendix, we discuss an alternate approach to obtaining parameters that relies on the properties of the weakly chaotic state.

C. Phase equations

A linear stability analysis of the laminar solution [Eq. (4)] to Eqs. (3), was carried out by Daviaud *et al.* [9]. They found that amplitude perturbations of the laminar state are damped, but that two phase unstable modes are observed for small wave-number perturbations. The condition for instability of these equations is given by

$$D=1+\alpha\beta+\kappa+\gamma(\beta\eta-\chi)<0. \tag{5}$$

It is interesting to note that the first two terms in Eq. (5) correspond to the Benjamin-Feir condition ($1+\alpha\beta<0$); thus the coupling to the second phase equation has the effect of modifying the onset of the phase instability.

The dynamics of the ϕ,ψ fields in the phase unstable region of the parameter space can then be expressed by the following dynamical equations, valid for small fluctuations in the phases:

$$\frac{\partial\psi}{\partial t}=(\beta\gamma-\delta)\,\frac{\partial\phi}{\partial x}+(1+\alpha\beta+\beta\eta\gamma)\,\frac{\partial^2\psi}{\partial x^2}+(\beta-\alpha)\left(\frac{\partial\psi}{\partial x}\right)^2, \tag{6a}$$

$$\frac{\partial\phi}{\partial t}=-2\,\eta\mu\,\frac{\partial\psi}{\partial x}+(\kappa-\gamma\chi)\,\frac{\partial^2\phi}{\partial x^2}+2\,\gamma\eta\,\frac{\partial\phi}{\partial x}\,\frac{\partial\psi}{\partial x}. \tag{6b}$$

Notice that the first coefficient in Eq. (6a) is the coupling term for the wave-number dependence of ω, a result that can be verified by setting $\phi=\phi_0+qx$ and $\psi=\psi_0+\omega t$. However, not all of the coefficients in Eq. (5) are known for the experiment. If a phase instability is the mechanism for the observed dynamics, then it would be preferable to be able to show that the fitted coefficients of a model satisfy Eq. (5). Equations (6) depend on six coefficients, a reduction from the original eight coefficients of Eq. (3), and may be a better choice of model equations to fit to the data gathered in the SSO state than the full model equations.

D. Least squares fit to model equations

Since in the weakly chaotic state one expects the system to probe a large portion of the phase space of the flow, it may be possible to extract estimates for the coefficients of the model equations. This experiment may be a good candidate for such an approach, which inevitably requires a large set of data for statistical analysis. Under the assumption that the model defined by Eq. (3) is appropriate, one may attempt a least squares fitting method to arrive at measured values for the coefficients. We report the results of such an analysis, including tests on numerical simulations, in the Appendix. Although some useful information can be obtained from this approach, experimental noise currently prevents a conclusive answer to the critical question: is the spatiotemporal chaos adequately described by the A-ϕ model and its associated phase instability?

The method consists in determining each term in the model equations independently at each point in space and time from measured data, then using this information to fit the coefficients of the model to the data. The model equations are linear in the coefficients, and fitting them is therefore straightforward. Tests on synthetic data generated by numerical integration recover the coefficients to better than 1%. The results are sensitive to noise, however, addition of 1% Gaussian noise to the data results in discrepancies in the estimates as large as 10% for some coefficients. This sensitivity to noise is carried over to the experimental data as well, where demodulation to obtain the slowly varying fields introduces a comparable amount of noise. In this case, only rough estimates can be made for the coefficients.

VI. DISCUSSION AND CONCLUSION

A. Oscillatory states

The rimming flow of a fluid inside a rotating cylinder demonstrates a number of interesting pattern-forming states

TABLE II. Coefficients determined by least squares fitting to numerical data. The parameters were chosen so as to produce a chaotic state, $D=-1.05$ ($\kappa=\gamma=\delta=0.25$).

Coefficient	Value	Fitted value—numerical data	Fitted with 1% rms noise
τ	1	1	1
μ	1	0.995 ± 0.002	0.87 ± 0.06
α_r	1	0.988 ± 0.002	0.86 ± 0.06
α_i	1	0.994 ± 0.002	0.85 ± 0.06
b_r	1	1.003 ± 0.002	0.88 ± 0.06
β_i	−1.2	−1.2058 ± 0.003	−1.19 ± 0.01
γ	2	1.994 ± 0.004	1.8 ± 0.1
δ	1.2	1.184 ± 0.003	1.14 ± 0.07

and transitions to spatiotemporal chaos. Instabilities of homogeneous, one-dimensional fronts include traveling pulses, long wavelength undulations, and spatially periodic states. Since the spatially periodic state is the most symmetric (and most common) of these bifurcations, we have explored the stability boundaries of this state in detail. Several of the phenomena observed are generic, while others are clearly specific to this system.

The most highly symmetric of the secondary instabilities of the cellular state is the transition to spatially subharmonic oscillations (Fig. 6). This transition breaks both space and time translation invariance, and is one of ten generic instabilities of a cellular state considered by Coullet and Iooss [2]. It is observed over a small range of volume fractions (region *C* of Fig. 4); the conditions for its stability are not known.

At higher volumes one observes a modified instability in which the oscillations are inherently broad and generally incommensurate with the periodic pattern [Figs. 8 and 9(b)]. This may be an example of another of the generic instabilities [2]. The existence of this state near that of the SSC state raises the important question of how the two oscillatory states (commensurate and incommensurate) and their bifurcations are related. Is there a ‘‘codimension-two’’ point in parameter space where these two states coincide with the cellular state?

The various transitions involving oscillatory states are strongly wave-number dependent. The cellular pattern is stable over a large range in Re-k space (Fig. 5). It is unstable with respect to both a wavelength-changing instability and the oscillatory instability just described. The wavelength dependence of the transition to oscillations is adequately described by the A-ϕ model (complex amplitude of oscillation coupled to a base pattern with spatially varying phase).

A solution to the full hydrodynamic equations may be needed for a better understanding of the oscillatory instability. However, one possible explanation arises from the following observations about the flow in the cellular state. If tracer particles are inserted into the flow, pairs of counter rotating vortices are observed in the fingers of the cellular front, with axes of rotation oriented normal to the surface of the cylinder (see, e.g., Ref. [6]). As the cells are compressed, these vortices may be forced to interact with a characteristic frequency that depends on their vorticity. Increasing compression of the cells leads to higher vorticity, and to a corresponding increase in the frequency of oscillation. Such a mechanism would be consistent with the results presented in Fig. 12. In addition, if the oscillatory interaction between vortices decays with increasing separation, then at lower wave number the oscillations should cease. This is generally consistent with our observations.

TABLE III. Fit of Eqs. (6) to simulated experimental data after demodulation of numerical data and 8 bit truncation. The simulation was done using the coefficients chosen for Table II. Slow length scale $L=37.5$, slow time scale $\tau=1$, fast time scale $\tau/30$, demodulation parameters: $k_0=68$, $dk=34$, $\omega_0=256$, $d\omega=128$, in units of the Fourier transform box size (512×2048).

Coefficient	Value	Fitted value—numerical data
τ	1	1
a_1	−3.6	−7.41 ± 0.04
a_2	−0.8	0.020 ± 0.006
a_3	−2.2	−1.42 ± 0.02
a_4	0.5	0.691 ± 0.003
a_5	−0.25	−0.22 ± 0.01
a_6	1.0	1.40 ± 0.01

B. Onset of spatiotemporal chaos

Three distinct types of spatiotemporal chaos are documented via their space-time Fourier spectra (Figs. 3 and 9). We focus on the transition from the homogeneous spatially subharmonic state to STC, where the transition is continuous and reversible. Near its onset, the STC state involves slow modulations of the cellular pattern, as indicated by the well-separated spectral peaks in Fig. 3. This clear separation of space and time scales justifies the use of slowly varying amplitude models. However, the spectral peaks broaden substantially as the rotation rate increases, and the fluctuating nucleation of additional cells limits the range of applicability of these models.

The model which was compared to the oscillatory state [Eq. (3)] is expected to be valid only very near the bifurcation from the cellular state, and it assumes that the secondary bifurcation to oscillations occurs far from the emergence of the cellular pattern. The more general sub-T model studied by De Wit and co-workers [7,8] drops the assumption of a saturated cellular state; in addition, the left- and right-going parts of the oscillatory amplitude are not assumed to be coupled. Near the codimension-two point for the bifurcations of the cellular and oscillatory modes (Turing and Hopf bifurcations), both pure cellular and oscillatory modes and subharmonic instabilities of these modes occur. Although most of these modes have not been observed in rimming flow, the broader approach of the sub-T model may eventually be useful, because it includes the primary cellular bifurcation.

Still, the A-ϕ model for the Hopf bifurcation [9] is simpler than the sub-T model, and yet shows the phenomena exhibited by the physical system near the onset of STC. These include a supercritical transition to oscillations; a wavelength dependence of the amplitude and frequency, and of the onset driving rate of the oscillatory instability; and a transition to spatiotemporal chaos with propagating compressions of the cellular pattern that are related to a locally de-

TABLE IV. Fit of Eqs. (6) to experimental data. One hundred files of size 512×2048 are included in the fit. Demodulation parameters: $k_0=34$, $dk=16$, $\omega_0=128$, $d\omega=64$.

τ	a_1 (cm/s)	a_2 (cm^2/s)	a_3 (cm^2/s)	a_4 (cm/s)	a_5 (cm^2/s)	a_6 (cm^2/s)
1	6.91 ± 0.07	0.002 ± 0.003	99.0 ± 1.3	9.3 ± 0.4	0.25 ± 0.14	-10.1 ± 0.4

pressed amplitude of oscillation.

In order to demonstrate conclusively that the phase instability of the model is actually the cause of the STC observed experimentally, we attempted a quantitative comparison by the least squares fitting process of the Appendix. However, the results are not decisive. Identification of a phase instability requires knowledge of several of the coefficients [Eq. (5)]. The combination a_2+a_5 of Table IV would have to be negative for phase instability, but appears to be weakly positive. We determined via numerical simulations that even modest amounts of experimental noise cause the fitting process to be rapidly degraded, and this situation makes a conclusive experimental test impossible.

Finally, one cannot rule out other possible explanations for the chaotic dynamics. For example, the transition to chaos could be the result of an instability of the cellular state that is coincident with but independent of the onset of oscillations. Perhaps the onset of STC is the result of phase instabilities in the base pattern (as seen, for example, in the WCI line of Fig. 5) extended to the oscillatory state at higher wave numbers. In such a case the analysis of the model equations [Eq. (3)] would not be valid. Though many lines of evidence indicate that the amplitude equation models can describe the onset of STC in this system, measurements at higher spatial resolution would be required to determine whether this is indeed the case, or whether, on the other hand, more elaborate models are required.

ACKNOWLEDGMENTS

We thank Anne De Wit, Annette Hosoi, and Bruce Gluckman for helpful discussions, and Stuart Edwards for discussions and software related to the fitting method presented in Appendix A. This work was supported by NSF Grant No. DMR-9319973.

APPENDIX

1. Fitting methods

In this appendix we address the question of whether the model parameters can be determined directly from the spatiotemporally chaotic SSO data by a least squares method, as Baker, Gollub, and Blackburn [10] did for *temporal* chaos given by coupled ordinary differential equations. Models of the type given in Eq. (3) may be expressed as a sum of terms

$$y(\mathcal{F})=\sum_{k=1}^{K} a_k X_k(\mathcal{F}), \tag{A1}$$

where X_k and y are nonlinear functions of $\mathcal{F}$, and a_k are coefficients to be determined from a set of N measurements $\mathcal{F}_i$. The model is linear in the fitting coefficients a_k [27]. For example, y could be $\partial A(x,t)/\partial t$ and X could be $|A|^2A$.

For each measurement $\mathcal{F}_i$ there is an associated residual R_i so that

$$R^2=\sum_{t=1}^{N}\left[\frac{y_i-\sum_{k=1}^{K} a_k X_k(\mathcal{F}_i)}{\sigma_i}\right]^2 .$$

The weighting σ_i is a measure of the uncertainty in the ith measurement of $\mathcal{F}$. In this analysis the data points are usually weighted equally, and the σ_i's are set to unity. The best fitting set (or vector) of parameters $\mathbf{a}=\{a_k\}$ is that for which the derivative of R^2 with respect to all a_k vanishes. We use a standard normal equation implementation of this minimization process. Finally, we note that the function y can be selected in various ways by rearranging the model equation to place a different term on the left hand side with coefficient unity.

In the following section, we show the results of applying the fitting method both to numerical data [obtained by integrating the model of Eq. (3)] and to experimental data. In the numerical case, excellent convergence is achieved and the parameters are obtained to a precision of 1% or better. If 1% rms of Gaussian noise is added to the signal, the parameters can still be determined, but less precisely (about 10–15 %). Applying the method to experimental data suffers from the difficulty that the slowly varying fields must first be obtained by demodulation. In this case, the results are disappointing.

2. Results of fitting

The least squares fitting approach was applied to synthetic chaotic data generated by direct numerical integration of Eq. (3). The coefficients were chosen to satisfy the stability condition $D<0$, and are given in Table II (in addition $\kappa=\gamma=\delta=0.25$). Here, the real coefficients α_i, β_r (set to unity in the model) are allowed to vary in the fit, and the coefficients α_i and β_i correspond to α, β of Eq. (3), respectively. The size of the space-time array was 10×2048×512. Three hundred fast time steps were computed per slow time unit τ, and every tenth time step was placed into the array. The slow spatial scale used was set to $L=37.5$ units (out of 512 total). The results of the fitting process applied to these numerical data are given in the third column of Table II, and are generally in excellent agreement with the actual values, better than 1%.

To perform a test of the method more closely analogous to dealing with experimental data, we added 1% rms of Gaussian random noise to the slowly varying fields. The results show that the method is sensitive to noise: errors of the order of 10% are found for the parameters. This sensitivity suggests that this direct method of extracting the coefficients of model equations for space-time data will be difficult to implement for noisy experimental data.

Finally, we simulate the effects of the demodulation process that must be applied to the experimental data. This is accomplished by using Eq. (1) to define the rapidly varying field $U(x,t)$ given the slowly varying fields $A(x,t)$ and $\phi(x,t)$ obtained from the numerical integration. We then truncate the resulting data to 8 bit precision and apply a window in Fourier space to recover the fields A, ϕ in a manner similar to what is done for the experimental data. In so doing, we recover the original fields to within approximately 1%. However, the results of fitting these (modulated and) demodulated data are not satisfactory. The result of the fit is sensitive to choice of demodulation parameter as well as to the separation between the slow and fast time scales.

Some improvement can be made by reducing the number of parameters to be fitted. Note that Eq. (6) is obtained from the stability analysis of the laminar states. A knowledge of the six coefficients of the phase equations in Eq. (6) is sufficient to test the hypothesis that the observed chaotic state is a result of a generic phase instability. In terms of the model coefficients in Eq. (3), the fitting coefficients are defined as follows: for Eq. (6a), $a_1=\beta\gamma-\delta$, $a_2=1+\alpha\beta+\beta\eta\gamma$, $a_3=\beta-\alpha$ and for Eq. (6b), $a_4=-2\eta\mu$, $a_5=\kappa-\gamma\chi$, and $a_6=2\gamma\eta$. The condition for phase instability of these equations is equivalent to the requirement that $a_2+a_5<0$. Since Eq. (6) are each independently of the form of Eq. (A1), they constitute two *independent* minimization problems, each of which has only three parameters.

When applied to *demodulated* numerical data, this reduced model gives more reliable results for several (but not all) of the coefficients than does the original model. The results of the fit are shown in Table III. Many of the coefficients are found with an accuracy of 10–100 %. Most troubling is the observation that the phase diffusion coefficient a_2 is found to be essentially zero, even though its actual value in creating the numerical data is negative. This difficulty probably reflects a need to improve the spatial resolution of the input data to improve the method, as discussed below.

A similar analysis applied to the *experimental* data is shown in Table IV, over 100 records of size 512×2048. The method converges quickly to the values shown (after about ten records). The coefficient a_1, which has been obtained independently (see Table I), differs from the measured value by a factor of 2. As we found for the demodulated numerical data, the phase diffusion coefficient is again essentially zero, which we presume to be an artifact of the demodulation.

A final consideration is whether higher order terms in Eq. (3) than those considered might be important. We have found that inclusion of higher order powers and derivatives in the model equations [Eq. (6)] for the phases did not result in statistically significant amplitudes for these new terms. Their inclusion also did not result in significant changes in the values of the coefficients in Table IV. It may be desirable to include the amplitudes of both A and U_0 explicitly in a model for the flow, as in the model proposed by De Wit and co-workers [7,8]. Tests comparing the experimental data to this more general model have not been performed, in part because of its greater complexity.

We conclude that the fitting process is at present suitable to the analysis of numerical data but cannot determine whether the A-ϕ model is adequate for describing the onset of STC in this experiment. Numerical tests suggest that the fitting process could possibly be improved if spatial data were available with higher resolution (say 2048 instead of 512 points). It also might be better to use the method in situations where the spatial variations are slower so that the derivatives can be computed more accurately. Best of all, experimental situations in which the fields described by the model equations are directly manifested (so that demodulation is unnecessary) would be more suitable candidates for this method.

---

[1] M. C. Cross and P. C. Hohenberg, Rev. Mod. Phys. **65**, 851 (1993).

[2] P. Coullet and G. Iooss, Phys. Rev. Lett. **64**, 866 (1990).

[3] P. Kolodner, S. Slimani, N. Aubry, and R. Lima, Physica D **85**, 165 (1995).

[4] M. Dennin, G. Ahlers, and D. S. Cannell, Science **272**, 388 (1996).

[5] D. P. Vallette, W. S. Edwards, and J. P. Gollub, Phys. Rev. E **49**, 4783 (1994).

[6] S. T. Thoroddsen and L. Mahadevan (unpublished).

[7] D. Lima, A. De Wit, G. Dewel, and P. Borckmans, Phys. Rev. E **53**, 1305 (1996).

[8] A. De Wit, D. Lima, G. Dewel, and P. Borckmans, Phys. Rev. E **54**, 261 (1996).

[9] F. Daviaud, J. Lega, J. Bergé, P. Coullet, and M. Dubois, Physica D **55**, 287 (1992).

[10] G. L. Baker, J. P. Gollub, and J. A. Blackburn, Chaos **6**, 528 (1996).

[11] F. Melo and S. Douady, Phys. Rev. Lett. **71**, 3283 (1993).

[12] M. J. Karweit and S. Corrsin, Phys. Fluids **18**, 111 (1975).

[13] K. J. Ruschak and L. E. Scriven, J. Fluid Mech. **76**, 113 (1976).

[14] F. M. Orr and L. E. Scriven, J. Fluid Mech. **84**, 145 (1978).

[15] J. A. Deiber and R. L. Cerro, Ind. Eng. Chem. Fundam. **15**, 102 (1976).

[16] R. E. Johnson, J. Fluid Mech. **190**, 321 (1988).

[17] R. E. Johnson, in *Coating Flow Stability in Rotational Molding*, edited by G. T. Yates, Engineering Science, Fluid Dynamics: A Symposium to Honor T. Y. Wu (World Scientific, Singapore, 1990), p. 435.

[18] L. Preziosi and D. D. Joseph, J. Fluid Mech. **187**, 99 (1988).

[19] J. Sanders, D. D. Joseph, and G. S. Beavers, J. Non-Newtonian Fluid Mech. **9**, 269 (1981).

[20] F. Melo, Phys. Rev. E **48**, 2704 (1993).

[21] R. Chicharro and R. Peralta-Fabi (unpublished).

[22] Manufactured by BitFlow, Inc.

[23] This same transition is also observed in region *B* of Fig. 4, but in that case, the transition is generally to another stable mode of stationary cells.

[24] J. Lega, Eur. J. Mech. B, Fluids **10**, 145 (1991).

[25] N. Bekki and K. Nozaki, Phys. Lett. **110A**, 133 (1985).

[26] T. B. Benjamin and J. E. Feir, J. Fluid Mech. **27**, 417 (1967).

[27] *Numerical Recipes: The Art of Scientific Computing*, edited by W. H. Press, B. P. Flannery, S. A. Teukolsky, and W. T. Vetterling (Cambridge University Press, New York, 1989).